Chinese Chemical Letters 36 (2025) 110701

Contents lists available at ScienceDirect

Chinese Chemical Letters

journal homepage: www.elsevier.com/locate/cclet

Performance optimization of aqueous Zn/MnO_2 batteries through the synergistic effect of PVP intercalation and GO coating

Shilong Li[a,1], Ming Zhao[a,1], Yefei Xu[b], Zhanyi Liu[b], Mian Li[b,*], Qing Huang[b], Xiang Wu[a,*]

[a] School of Materials Science and Engineering, Shenyang University of Technology, Shenyang 110870, China
[b] Zhejiang Key Laboratory of Data-Driven High-Safety Energy Materials and Applications, Ningbo Institute of Materials Technology and Engineering, Chinese Academy of Sciences, Ningbo 315201, China

ARTICLE INFO

Article history:
Received 14 October 2024
Revised 26 November 2024
Accepted 29 November 2024
Available online 30 November 2024

Keywords:
Aqueous zinc ion batteries
Cathode
MnO_2
Cycle stability
High capacity

ABSTRACT

Manganese dioxide (MnO_2) electrode material possesses the advantages of high energy density, structural diversity and high modification potential. This allows it become one of the important cathodes for aqueous zinc ion battery. However, the applications are limited by the poor electrical conductivity, narrow layer spacing and the ease of dissolution. Herein, we prepare MnO_2-PVP@0.03GO composites by the co-modification of polyvinylpyrrolidone (PVP) pre-insertion layer and graphene oxide (GO) self-assembly layer. The Zn//MnO_2-PVP@0.03GO cells deliver a discharge specific capacity of 442 mAh/g at a current density of 0.2 A/g. It also maintains 100% capacity for 1000 times cycling at 1 A/g. The assembled soft package batteries demonstrate superior flexibility and adaptability under different bending conditions.

Aqueous zinc-ion batteries (AZIBs) are a new type of energy storage devices, which adopt an aqueous electrolyte system, avoiding the safety hazards of flammable and explosive organic electrolytes [1,2]. It demonstrates a broad application prospect in the fields of vehicles, electric transport and consumer electronics [3]. Zn anode is an ideal for aqueous metal ion batteries due to its high theoretical capacity (820 mAh/g), low redox potential (–0.76 V *vs.* SHE) and abundant resources [4,5]. However, the cathode materials are prone to structural changes or dissolution during charging and discharging, resulting in their unstable cycling performance [6,7]. Therefore, the selection and optimization of cathode are essential to improve the battery performance [8]. Currently, it main includes Mn/V-based compounds, Prussian blue compounds and polymers [9–11]. Among them, MnO_2 material is a hot research topic due to its diverse structure (α-MnO_2, β-MnO_2, γ-MnO_2, δ-MnO_2), high energy density and easy preparation [12]. In particular, the large spacing of δ-MnO_2 layers (≈7.0 Å) provides the possibility of embedding and detaching Zn^{2+} [13]. This avoids the problems of structural rearrangement and crystalline phase changes. Nevertheless, the δ-MnO_2 electrode shows sluggish kinetics behavior during the electrochemical reactions [14]. This is mainly caused by the Jahn-teller effect which leads to a severe solubilization of Mn^{2+} in aqueous electrolyte [15] and the slow desolation of hydrated $[Zn(H_2O)_6]^{2+}$ ions and strong coulombic interactions between Zn^{2+}/Mn^{2+} [16]. The collapse of the host lattice structure leads to rapid capacity decay and poor cyclic stability when Zn^{2+}/H^+ is co-embedded in the redox process [17].

To increase the structural defects, pre-insertion engineering has become a groundbreaking attempt [18,19]. Wang *et al.* reported a pre-insertion layer of Na^+. The Zn//NMOH cells possesses a specific capacity of 278 mAh/g at 1 C [20]. However, when confronted with abundant Zn^{2+} and cations, the "pillar" ions can be replaced due to weak electrostatic interactions in the Helmholtz plane [21]. To enhance the cycling stability, the cladding technology can mitigate the dissolution of Mn^{2+} by constructing a surface coating [22]. It avoids the direct contact between electrolyte and electrode. Xiao and coworkers constructed a homogeneous hydrophobic amino-propyl phosphonic acid (AEPA) layer on the surface of manganese dioxide structure [23]. The MnO_2@AEPA cathode provides 223 mAh/g at 0.5 A/g and 97% capacity retention at 1 A/g after 1700 times cycling. However, the artificial coatings are usually a few micro-meters thick, with weak adhesion, high resistance to ion transfer and prone to rupture during long-term cycling [24]. In addition, some energy-intensive calcination techniques risk damaging the pristine structure [25].

Herein, we have combined doping and coating technologies to modulate the interlayer configuration through polyvinylpyrrolidone (PVP) pre-intercalation and hydrophobic graphene oxide (GO) cladding layers on the surface of MnO_2 electrode. PVP effectively improves the conductivity of the electrode and also acts as a

* Corresponding authors.
E-mail addresses: limian@nimte.ac.cn (M. Li), wuxiang05@sut.edu.cn (X. Wu).
[1] These authors contributed equally to this work.

https://doi.org/10.1016/j.cclet.2024.110701
1001-8417/

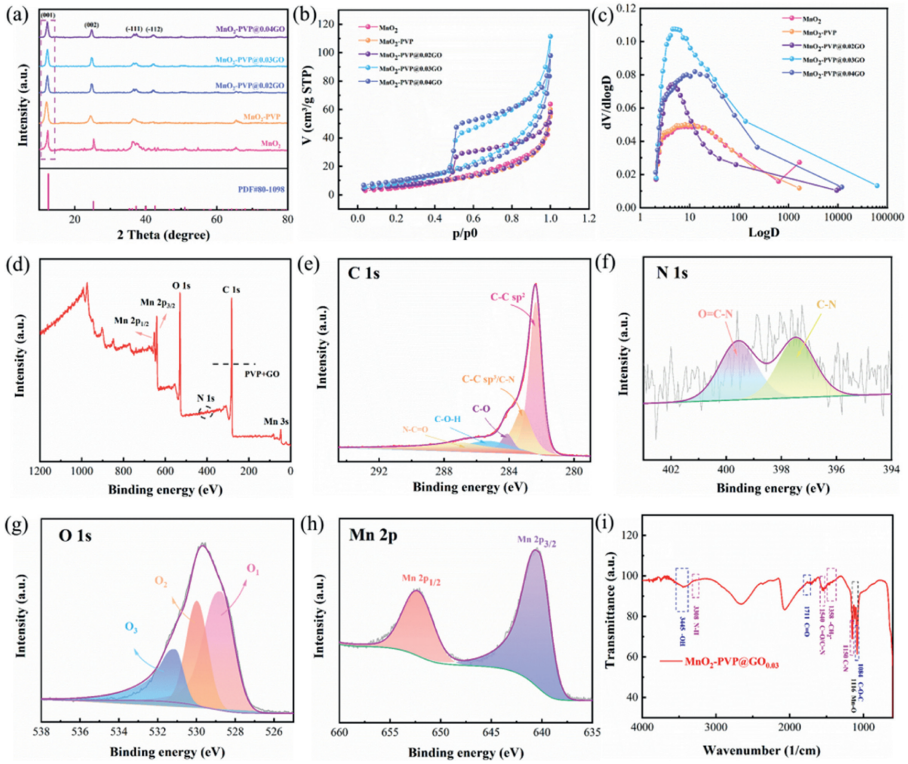

Fig. 1. Structural characterization: (a) XRD patterns. (b, c) N_2 adsorption/desorption isotherms and pore size distribution curves. (d) XPS survey spectrum of MnO_2-PVP@0.03GO materials. (e) C 1s, (f) N 1s, (g) O 1s and (h) Mn 2p spectra. (i) FTIR spectra.

"pillar" ion to mitigate the damage to the material structure caused by volume expansion. Thus, it helps to maintain the structural integrity and improve the redox reversibility. The prepared MnO_2-PVP@0.03GO electrodes deliver a specific capacity of 442 mAh/g at a current density of 0.2 A/g. The capacity retention of the assembled coin and soft pack batteries are 100% and 98% after 1000 times cycling at 1 A/g, respectively.

The chemicals used in the experiments are all analytical grade (AR) without any purification. A typical hydrothermal route was used for the synthesis of MnO_2-PVP@0.03GO nanoflowers. 0.225 g $KMnO_4$, 0.8875 g KNO_3, and 0.05 g PVP powder were put into 50 mL of deionized (DI) water and stirred at room temperature for 30 min. The mixed solution was then transferred to an 80 mL Teflon-lined autoclave and heated at 160 °C for 12 h. After cooling to room temperature, it was washed several times with anhydrous ethanol and DI water and dried overnight in a vacuum chamber at 60 °C. The collected powder was named MnO_2-PVP. 0.1 g of MnO_2-PVP powder and 0.02, 0.03 and 0.04 mg/mL graphene oxide (GO) solutions were stirred at 75 °C for 1 h. Subsequently, they were placed into a Teflon-lined autoclave at 180 °C for 3 h. The samples obtained were marked as MnO_2-PVP@0.02GO, MnO_2-PVP@0.03GO and MnO_2-PVP@0.04GO. For comparison, the samples were labelled as MnO_2 samples without the introduction of PVP and GO.

The prepared powder, Super P and polytetrafluoroethylene (PVDF) were ground in the ratio of 7:2:1 by weight. Then, the appropriate amount of *N*-methyl-l-2-pyrrolidone (NMP) was added and they were pressed onto carbon paper and dried at 60 °C. The CR2032 type cells were assembled by the obtained cathode, glass fiber diaphragm, zinc foil and electrolyte (2 mol/L $ZnSO_4$ + 0.2 mol/L $MnSO_4$). For the flexible device, the MnO_2-PVP@0.03GO cathode and zinc foil were separated by a hydrogel electrolyte (PAM) and encapsulated with an aluminum plastic film. The average loading mass of the cathode material is 1.5 mg. The electrochemical performance was then determined using a Neware battery system (CT-4008T) with a potential range from 0.8 V to 2.0 V. Finally, we studied the cyclic voltammetry (CV) curves and electrochemical impedance spectroscopy (EIS) in a CHI660E workstation.

The crystal structure was then studied by an X-ray powder diffractometer (XRD, Rigaku Ultima IV, Japan, Cu Kα 1.54178 Å, 40 kV). The specific surface area and the porosity of the samples were determined by the N_2 adsorption-desorption isotherms. The material composition is detected by Fourier transform infrared (FTIR) spectroscopy using KBr pellets (Thermo Scientific Nicolet iS20, USA). The chemical bonding of the samples was studied by X-ray photoelectron spectroscopy (XPS, Thermo Scientific K-Alpha, USA). Finally, the morphology of the products was observed by scanning electron microscope (SEM, Hitachi, S-3400N) and high-resolution transmission electron microscope (HRTEM, JEM-2100 PLUS).

Firstly, the crystal structure of the samples is confirmed by XRD, as shown in Fig. 1a. All the diffraction peaks are indexed to MnO_2 phase (JCPDS No. 80-1098). The peaks located at 12.4°, 25.2°, 36.3° and 42.5° correspond to the (001), (002), ($\bar{1}$11), ($\bar{1}$12) crystal planes, respectively. Notably, they are slightly shifted to lower angles which confirm the embedding of the PVP. However, the peak intensities of the latter are weaker than those of the former due to the GO coating.

Figs. 1b and c show the N_2 isotherms of five samples with typical type IV hysteresis lines. Their specific surface areas are 25.350, 30.842, 39.621, 43.091 and 37.254 cm^2/g, which correspond to the total pore volumes of 0.075, 0.0823, 0.122, 0.135 and 0.107 cm^3/g, respectively, as shown in Fig. 1c. The increased specific surface area offers many active sites for the reaction, thus enhancing the reaction rate. The moderate pore size facilitates ion transport and minimizes volume fluctuations during the reaction [26]. XPS is then used to study the valence distribution of the MnO_2-PVP@0.03GO samples. Signal peaks for N 1s, C 1s, Mn 2p, and O 1s can be found in the total spectrum (Fig. 1d). In Fig. 1e, the C 1s spectra are

fitted to C-C sp^2 (282.3 eV), C-C sp^3 (283.1 eV), C-O (284.1 eV), C-O-H (285.35 eV) and N-C=O (287.2 eV) [27]. The appearance of N-C=O is attributed to the introduction of PVP. From N 1s spectra, the peaks located at 399.5 and 397.9 eV belong to the O=C-N and C-N bonds (Fig. 1f) [28]. Fig. 1g shows the O 1s spectra, which can be convolved into O_1 (Mn-O-Mn 528.9 eV), O_2 (Mn-O-H 530.1 eV) and O_3 (H-O-H 531.3 eV) bonds [29,30]. The Mn 2p spectra (Fig. 1h) can be fitted to two peaks located at 640.7 and 652.1 eV, which correspond to Mn $2p_{3/2}$ and Mn $2p_{1/2}$, respectively [31]. It is related to the Mn-O vibrations of the [MnO_6] octahedron [32]. The signals peaks belong to C=O, -CH_2-, C-N in PVP [33] and C-O-C, C=O, -OH- in GO [34] can be detected in FTIR (Fig. 1i). This indicates that PVP and GO are successfully introduced.

After that, we obverse the morphology of the resulting samples by SEM. The results show that they present the shape of microspheres assembled from nanosheets (Figs. 2a–e). The hybrid sheet structure favors the increase of their specific surface area, while the coating of GO does not change the morphological characteristics of the material. As shown in Fig. 2f, the Mn, C, N, and O elements are uniformly distributed along the sample surface. It can be seen from the HRTEM (Fig. 2g) that 0.3082 nm of crystal spacing can be indexed to the (113) crystalline surface. This proves the successful embedding of PVP. The GO coating on the outer surface of the sample is clearly observed in Fig. 2h. According to Fig. 2i, the lattice spacing of 0.2398 nm corresponds to the ($\bar{1}12$) crystal plane. This amorphous feature confirms the formation of a carbon layer, which promotes fast the transfer of electrons.

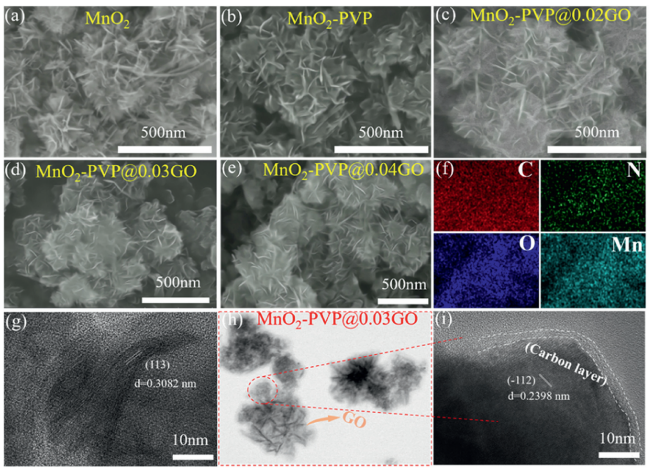

Fig. 2. Morphology characterization of five samples: (a-e) SEM images. (f) The corresponding elements mapping. (g-i) HRTEM images of MnO_2-PVP and MnO_2-PVP@0.03GO.

To evaluate the electrochemical performance, the prepared electrodes are assembled into some button cells. In Fig. 3a, two pairs

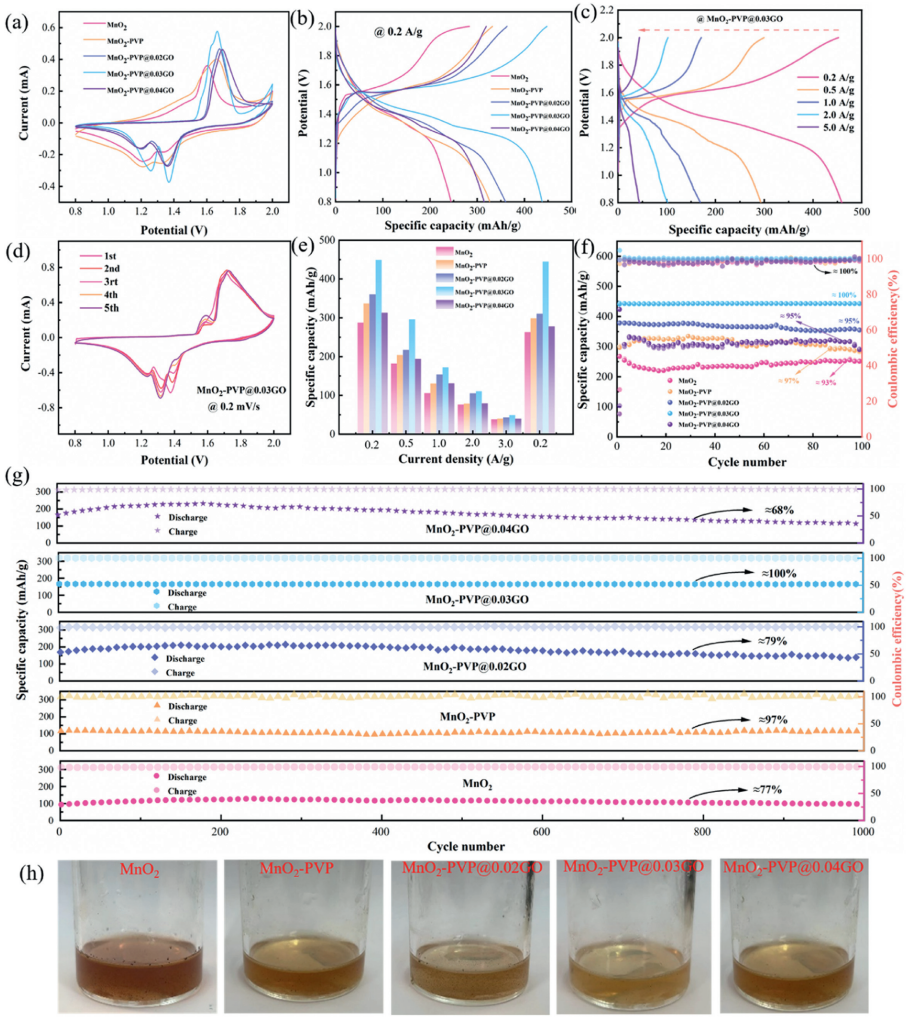

Fig. 3. Electrochemical performance: (a) CV curves at 0.2 mV/s. (b, c) GCD curves. (d) Cycle curves at 0.2 A/g. (e) Rate capability and (f) short-term cycle at 0.2 A/g. (g) Long-term cycle at 1.0 A/g. (h) Mn^{2+} dissolution after cycling

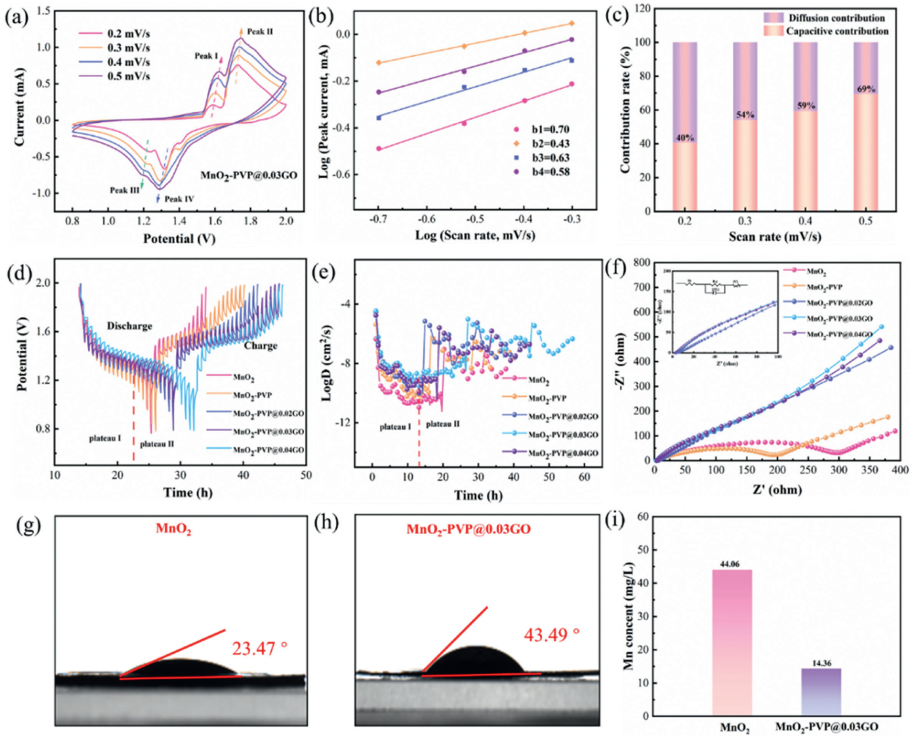

Fig. 4. Electrochemical reaction kinetics of Zn//MnO_2-PVP@0.03GO batteries: (a) CV curves at various scan rates. (b) Fitting plots of log(i) and log(v). (c) Capacitive contribution ratio at various scan rates. (d, e) GITT curves. (f) EIS. (g, h) Contact angle of the electrolyte (2 mol/L $ZnSO_4$ with 0.2 mol/L $MnSO_4$) on the MnO_2 and MnO_2-PVP@0.03GO. (i) ICP.

of redox peaks appear in all the CV curves, which demonstrate the reaction process is a two-step reaction. Among them, MnO_2-PVP@0.03GO sample possesses a large integration area, indicating its excellent electrochemical activity and high charge capacity. From the GCD curves, the capacity decreases with increasing current density (Figs. 3b and c). At the same time, the two discharge plateaus correspond to the corresponding CV curves. Fig. 3d shows the CV curves at a scan rate of 0.2 mV/s. Two pairs of redox peaks located at 1.586/1.712 eV and 1.327/1.405 eV, which correspond to the insertion/de-insertion process of Zn^{2+} and H^+, respectively. In addition, the curves of the first five cycles almost overlapped, indicating the high reversibility of the cells. From Fig. 3e, the Zn//MnO_2-PVP@0.03GO batteries offer the discharge specific capacity of 448, 296, 172, 110 and 47 mAh/g at current densities of 0.2, 0.5, 1.0, 2.0 and 3.0 A/g, respectively. It can be found that the electrode capacity is significantly increased by the synergistic effect of PVP and GO compared to the un-doped sample.

We further investigate the cycling stability of the cells at different current densities, as shown in Figs. 3f and g. The results show that the cyclic stability is greatly improved by doping with PVP, which is especially obvious at 1 A/g. Meanwhile, GO cladding with appropriate concentration can achieve 100% stability. It indicates that the stability of the layered MnO_2 structure is fully guaranteed under the dual interaction of PVP and GO. In addition, we can accelerate the dissolution of substances on the electrode sheet using an electrochemical strategy (Fig. 3h). in a three-electrode system: A Hg/HgO electrode is used as the reference electrode, the counter electrode is a Pt sheet electrode, the working electrode is a prepared electrode, and the electrolyte is 2 mol/L $ZnSO_4$ + 0.2 mol/L $MnSO_4$ solution. We apply a current of 50 mA to the working electrode sheet and perform the charging and discharging process for 200 s. It can be found that the MnO_2-PVP@0.03GO electrode dissolves less and lighter in color compared to the other samples, which proves that PVP and GO can effectively slow down the dissolution of Mn^{2+}.

Electrochemical kinetics is a key metric to further understand the storage behavior of Zn^{2+}. Fig. 4a shows the CV curves of the MnO_2-PVP@0.03GO electrode at 0.1–0.5 mV/s. The redox peaks also shift as the sweep rate increases. The equation for the relationship between sweep speed (v) and current (i) can be calculated as below [35]:

$$i = av^b \tag{1}$$

The value of b can be obtained from a linear fit (Fig. 4b). The b values of the four peaks are 0.43, 0.58, 0.63 and 0.70. When b value is between 0.5 and 1, it indicates that the cell is dominated by both ionic and pseudocapacitive diffusion. Subsequently, in Fig. 4c, the capacitance contributions for surface control and diffusion control are obtained from the following equations [36]:

$$i(V) = k_1 v + k_2 v^{1/2} \tag{2}$$

where $k_1 v$ and $k_2 v^{1/2}$ denote the diffusion and capacitance control processes, respectively. The latter increases from 40% to 69% of the total charge storage as the sweep speed increases from 0.2 mV/s to 0.5 mV/s. As shown in Figs. 4d and e, we determine the diffusion coefficient of Zn^{2+} (D_{Zn}) by GITT according to Eq. 3 [37]:

$$D = \left(4L^2\right)/\pi\tau\left(\Delta E_s/\Delta E_t\right)^2 \tag{3}$$

where τ is the relaxation time; ΔE_s is the pulse-induced voltage change and ΔE_t is the voltage change for constant current charging (discharging). In this range, the discharge process is divided into two plateau regions. The plateau I mainly correspond to the embedding of H^+, while the plateau II is dominated by the embedding of Zn^{2+}. The ion diffusion coefficients of plateau I are between 10^{-8} cm^2/s and 10^{-7} cm^2/s, while the ion diffusion coefficients of plateau II are about 10^{-10} cm^2/s. This is caused by the large difference in the radii of H^+ and Zn^{2+}. In a certain frequency range (0.01 Hz–100 kHz), we study the EIS of the cell (Fig. 4f). The semicircle in the high frequency region corresponds to the charge transfer resistance (R_{ct}), whose magnitude is proportional to the

Table 1
Initial capacity of various cathode materials.

Materials	Potential window (V)	Current density (A/g)	Specific capacity (mAh/g)	Cycling stability	Energy density (Wh/kg)	Ref.
O_d-HVO	0.2–1.6	0.2	337	85%	228	[39]
O_d-MnO_2	1.0–1.8	0.2	345	94%	235	[40]
$(NH_4)_2V_{10}O_{25}$	1.0–1.8	0.1	442	63%	243.2	[41]
S-MnO_2	0.8–1.8	0.2	324	≈77%	194.4	[42]
K-δ-MnO_2	1.0–1.8	0.1	270.3	≈46%	108.1	[43]
MnO_2@PANI	1.0–1.85	0.2	342	82%	199.5	[44]
δ-MnO_2 ND_S	1.0–1.9	0.1	335	86.2%	233	[45]
V-doped MnO_2	1.0–1.8	0.066	266	-	-	[46]
PVP-MnO_2	0.8–1.8	0.25	309	100%	154.5	[47]
MnO_2@AEPA	0.8–2.0	0.5	223	97%	133.8	[23]
δ-MnO_2-400	0.8–2.0	0.2	442	100%	265.5	This work

impedance. The series resistance (R_s) is the intercept between the curve and the x-axis and represents the solution internal resistance between the cell and the electrolyte. Meanwhile, the ion diffusion resistance (Z_w) appears as a line slope in the low frequency region.

In contrast, the MnO_2-PVP@0.03GO electrode possesses a small radius and a high slope. The results suggest that the modification of PVP and GO can improve the electrical conductivity. The energy (E (Wh/kg)) and power (P (W/kg)) density of a battery can be expressed by the following equations [38]:

$$E = QU/2m \quad (4)$$

$$P = iU/2m \quad (5)$$

where Q is the discharge specific capacity, U represents the potential difference, I refer to the current density, and m denotes the electrode loading mass. It can be concluded that the device presents an energy density of up to 265.2 Wh/kg at 120 W/kg. Table 1 lists the initial discharge capacities of several electrodes [23,39–47]. It can be observed that the prepared materials show excellent electrochemical performances. Figs. 4g and h show the water contact angle data, where the interfacial properties of MnO_2 and MnO_2-PVP@0.03GO cathodes are investigated respectively. The contact angle of the latter with the electrolyte (2 mol/L $ZnSO_4$+0.2 mol/L $MnSO_4$) reaches 43.49°, which is higher than that of the former (23.47°). It indicates that high hydrophobicity is beneficial to preventing the direct contact between the electrode and the electrolyte. This inhibits the dissolution of Mn^{2+} and improves the reversibility of the MnO_2 cathode, which can be confirmed according to previous reports [48,49]. Meanwhile inductively coupled plasma emission spectroscopy (ICP-OES) verified this result again [50]. We used 2 mol/L $ZnSO_4$ as electrolyte to eliminate the effect of Mn^{2+} additive. As shown in Fig. 4i, the content of Mn dissolved from MnO_2-PVP@0.03GO after cycling is only 1/3 of the original electrode under the same conditions.

Then we use *ex-situ* XRD test to explore the energy storage mechanism and ion transfer behavior of MnO_2-PVP@0.03GO electrodes (Fig. 5a). The (001) crystal surface shifts significantly during the charging and discharging process. Also, we find the H^+ intercalation $Zn_4SO_4(OH)_6{\cdot}0.5H_2O$ product (JCPDS No. 44-0674) [42]. However, the products arising from Zn^{2+} embedding are not observed, which can be attributed to the amorphous structure of Zn^{2+}. It is noteworthy that the newly formed $Zn_4SO_4(OH)_6{\cdot}3H_2O$ (JCPDS No. 039-0689) product appear due to the partial loss of H^+ and deep discharging [47]. The repeated generation and dissolution of the two products during charging and discharging confirms the excellent redox reversibility. Subsequently, we study the elemental valence states of the MnO_2-PVP@0.03GO cathode in the fully charged and discharged states. From the XPS in Fig. 5b, the peak intensities of Zn $2p_{1/2}$ and Zn $2p_{3/2}$ in the fully discharged state are significantly higher than those in the fully charged state. This

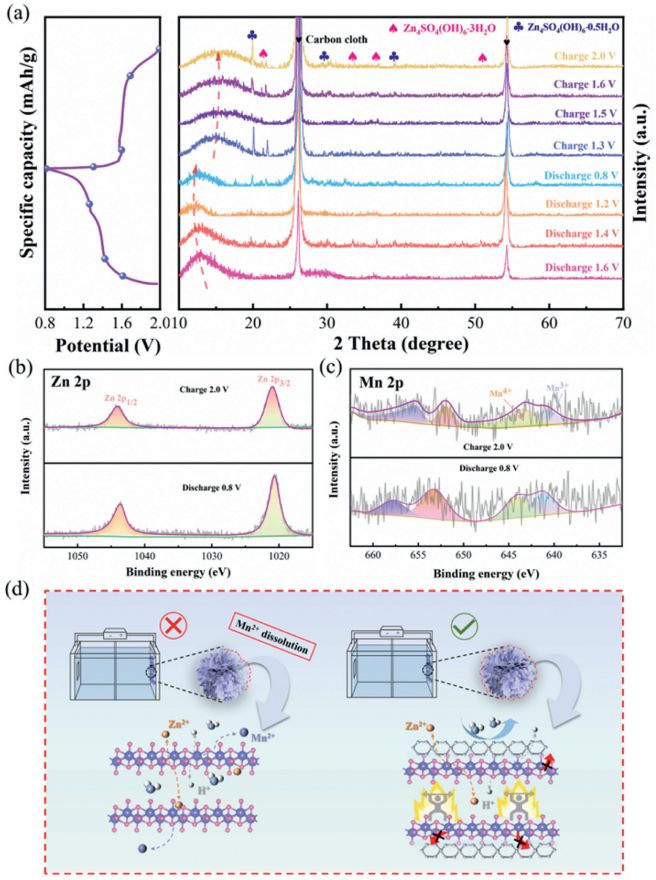

Fig. 5. Structural and morphology characterizations. (a) *Ex-situ* XRD patterns at various charge/discharge states. (b) Zn 2p. (c) Mn 2p. (d) Schematic diagram of the protection mechanism.

further confirms the existence of reversible insertion/de-insertion of Zn^{2+}. In Fig. 5c, the Mn^{4+} signal is followed by the Mn^{3+} signal. After charging to 2.0 V, the Mn^{4+} is stronger than the Mn^{3+} signal peak, which is consistent with previous report [51]. The structure and electrochemical mechanism of the cathode material are shown in Fig. 5d. PVP acts as a "pillar" can prevent the structure from collapsing, while the cladding layer of GO inhibits the dissolution of Mn^{2+}. The synergistic effect largely improves the performance of the cathode material.

Finally, we assemble some flexible cells by MnO_2-PVP@0.03GO electrode, zinc foil and hydrogel. The schematic diagram of the battery is illustrated in Fig. 6a. The GCD curves (Fig. 6b) show that the discharge time is not decreasing with the increase of folding angle, which indicates the satisfactory mechanical properties. Fig. 6c

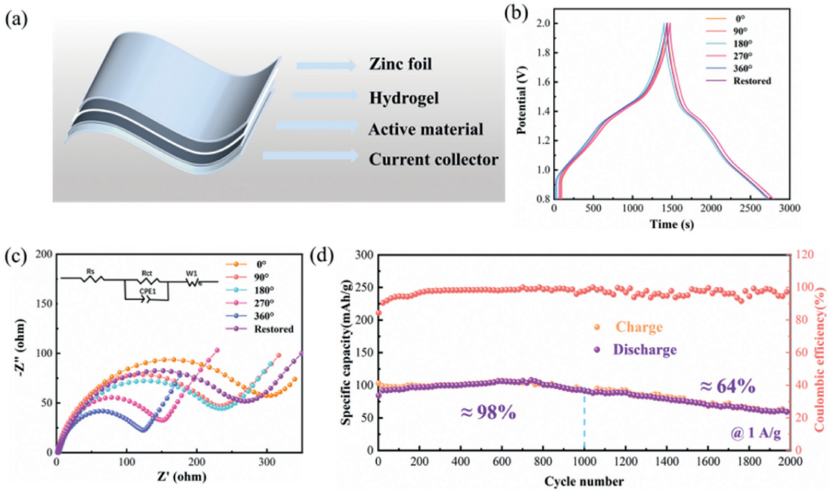

Fig. 6. (a) Flexible device structure schematic. (b) GCD. (c) EIS. (d) Long-term cycles at 1 A/g.

delivers the EIS of the battery at different folding angles. The resistance decreases as the folding angle increases. This can be attributed to the full contact of the hydrogel with the electrodes. When restored to 0°, the corresponding R_{ct} value is nearly the original state. Moreover, the capacity retention of the Zn//MnO_2-PVP@0.03GO flexible cell reaches 98%/64% after 1000/2000 cycles at 1 A/g (Fig. 6d).

In summary, we have prepared PVP and GO layer decorated MnO_2 electrode materials by a simple hydrothermal strategy. PVP not only acts as a pillar to effectively enhance H^+ transport, but also prevents structural collapse caused during charging and discharging. GO is firmly adhered to the surface of MnO_2 and acts as a protective layer to isolate the aqueous electrolyte from the cathode, which significantly inhibits the Mn^{2+} dissolution. The synergistic effect of PVP and GO imparts fast proton kinetics and promotes the cycling stability. The MnO_2-PVP@0.03GO electrode presents high specific capacity and demonstrates excellent cycling stability at a current density of 0.2 A/g. In addition, the flexible pack batteries show great potential in energy storage field due to their excellent mechanical stability and long cycle life.

Declaration of competing interest

The authors declare that they have no known competing financial interests or personal relationships that could have appeared to influence the work reported in this paper.

CRediT authorship contribution statement

Shilong Li: Writing – original draft, Visualization, Validation, Software, Methodology, Formal analysis, Data curation, Conceptualization. **Ming Zhao:** Writing – original draft, Visualization, Validation, Software, Methodology, Formal analysis, Data curation, Conceptualization. **Yefei Xu:** Visualization, Validation, Software, Data curation. **Zhanyi Liu:** Validation, Investigation, Data curation. **Mian Li:** Software, Investigation, Funding acquisition, Formal analysis, Data curation. **Qing Huang:** Writing – review & editing, Validation, Supervision, Resources. **Xiang Wu:** Writing – review & editing, Supervision, Resources, Project administration, Investigation, Funding acquisition, Data curation, Conceptualization.

Acknowledgment

The work is supported by National Natural Science Foundation of China (No. 52172218).

References

[1] Y. Liu, X. Wu, Chin. Chem. Lett. 33 (2022) 1236–1244.
[2] C. Li, X. Xie, S. Liang, J. Zhou, et al., Energy Environ. Mater. 3 (2020) 146–159.
[3] Y. Liu, Y. Liu, X. Wu, et al., J. Colloid Interface Sci. 628 (2022) 33–40.
[4] Z. Pei, Nano Res. Energy 1 (2022) e9120023.
[5] X. Guo, C. Wang, W. Wang, et al., Nano Res. Energy 1 (2022) e9120026.
[6] L. Chen, Q. An, L. Mai, Adv. Mater. Interface. 6 (2019) 1900387.
[7] C. Su, X. Gao, K. Liu, et al., Nano Res. Energy 3 (2024) e9120094.
[8] K. Yao, S. Xu, Y. Yang, et al., Inf. Funct. Mater. 1 (2024) 242–263.
[9] S. Liu, L. Kang, J. Kim, et al., Adv. Energy Mater. 10 (2020) 2000477.
[10] Y. Liu, X. Wu, J. Energy Chem. 87 (2023) 334–341.
[11] C. Zhao, Y. Liu, S. Li, et al., Chin. Chem. Lett. (2024), doi:10.1016/j.cclet.2024.110185.
[12] V. Mathew, B. Sambandam, S. Kim, ACS Energy Lett. 5 (2020) 2376.
[13] X. Jia, C. Liu, Z.G. Neale, et al., Chem. Rev. 120 (2020) 7795–7866.
[14] D. Chen, M. Lu, D. Cai, et al., J. Energy Chem. 54 (2021) 712–726.
[15] Y. Zuo, T. Meng, H. Tian, et al., ACS Nano 17 (2023) 5600–5608.
[16] B. Sambandam, V. Mathew, S. Kim, et al., Chem 8 (2022) 924–946.
[17] T. Xiong, Z. Yu, H. Wu, et al., Adv. Energy Mater. 9 (2019) 1803815.
[18] Y. Li, D. Zhang, S. Huang, et al., Nano Energy 85 (2021) 105969.
[19] J. Post, Proc. Natl. Acad. Sci. U. S. A. 96 (1999) 3447–3454.
[20] D. Wang, L. Wang, G. Liang, et al., ACS Nano 13 (2019) 10643–10652.
[21] P. Simon, Y. Gogotsi, Nat. Mater. 20 (2021) 1597–1598.
[22] N. Li, Z. Hou, S. Liang, et al., Chem. Eng. J. 452 (2023) 139408.
[23] X. Xiao, L. Zhang, W. Xin, et al., Small 20 (2024) 2309271.
[24] Y. Fu, Q. Wei, G. Zhang, et al., Adv. Energy Mater. 8 (2018) 1801445.
[25] X. Li, Q. Zhou, Z. Yang, et al., Energy Environ. Mater. 6 (2023) e12378.
[26] X. Chen, L. Wang, H. Li, et al., J. Energy Chem. 38 (2019) 20–25.
[27] S. Deng, Z. Tie, F. Yue, et al., Angew. Chem. Int. Ed. 61 (2022) e202115877.
[28] I. Safo, C. Dosche, M. Özaslan, ChemPhysChem 20 (2019) 3010–3023.
[29] X. Liao, C. Pan, Y. Pan, et al., J. Alloys Compd. 888 (2021) 161619.
[30] Y. Liu, P. Zhang, J. Phys. Chem. C 121 (2017) 23488–23497.
[31] X. Li, Q. Zhou, Z. Yang, et al., Energy Environ. Mater. 6 (2023) e12378.
[32] N. Li, Z. Hou, S. Liang, Y. Cao, et al., Chem. Eng. J. 452 (2023) 139408.
[33] J. Zhang, W. Li, J. Wang, et al., Angew. Chem. Int. Ed. 62 (2023) e202215654.
[34] Q. Wang, Y. Yang, Mater. Sci. 10 (2020) 819–823.
[35] Y. Liu, X. Wu, Nano Energy 127 (2024) 109809.
[36] M. Zhao, S. Li, X. Wu, Adv. Mater. Technol. 9 (2024) 2400125.
[37] J. Huang, Z. Wang, M. Hou, et al., Nat. commun. 9 (2018) 2906.
[38] M. Zhao, S. Li, X. Wu, et al., iScience 27 (2024) 110926.
[39] Z. Zhang, B. Xi, X. Wang, et al., Adv. Funct. Mater. 31 (2021) 2103070.
[40] T. Xiong, Z. Yu, H. Wu, et al., Adv. Energy Mater. 9 (2019) 1803815.
[41] M. Zhao, S. Li, A. Umar, et al., Mater. Today Chem. 33 (2023) 101686.
[42] Y. Zhao, P. Zhang, J. Liang, et al., Energy Storage Mater. 47 (2022) 424–433.
[43] Q. Xie, G. Cheng, T. Xue, et al., Mater. Today Energy 24 (2022) 100934.
[44] N. Li, Z. Hou, S. Liang, et al., Chem. Eng. J. 452 (2023) 139408.
[45] H. Tang, W. Chen, N. Li, et al., Energy Storage Mater. 48 (2022) 335–343.
[46] M. Alfaruqi, S. Islam, V. Mathew, et al., Appl. Surf. Sci. 404 (2017) 435–442.
[47] A. Zhang, R. Zhao, Y. Wang, et al., Angew. Chem. Int. Ed. 62 (2023) e202313163.
[48] T. Cetinkaya, M. Tokur, S. Ozcan, et al., Mater. Today: Proc. 2 (2015) 4223–4228.
[49] X. Huang, K. Shi, J. Yang, et al., J. Power Sources 356 (2017) 72–79.
[50] J. Heo, S. Chong, S. Kim, et al., Batt. Supercap. 4 (2021) 1881–1888.
[51] S. Li, M. Zhao, D. Zhang, et al., Cryst. Growth Des. 23 (2023) 8156–8162.